PL-TR-93-2010

HANDBOOK FOR THE USAF SPACE ENVIRONMENT STANDARD (MIL-STD-1809)

The Aerospace Corporation
El Segundo, CA 90245

January 1993

Scientific Report No. 2

PHILLIPS LABORATORY
Directorate of Geophysics
AIR FORCE MATERIEL COMMAND
HANSCOM AIR FORCE BASE, MA 01731-3010

"This technical report has been reviewed and is approved for publication"

Allen G. Rubin
(Signature)
ALLEN G. RUBIN
Contract Manager

(Signature)
DAVID A. HARDY
Branch Chief

(Signature)
WILLIAM SWIDER
Asst Division Director

This report has been reviewed by the ESC Public Affairs Office (PA) and is releasable to the National Technical Information Service (NTIS).

Qualified requestors may obtain additional copies from the Defense Technical Information Center. All others should apply to the National Technical Information Service.

If your address has changed, or if you wish to be removed from the mailing list, or if the addressee is no longer employed by your organization, please notify PL/TSI, Hanscom AFB, MA 01731-3010. This will assist us in maintaining a current mailing list.

Do not return copies of this report unless contractual obligations or notices on a specific document requires that it be returned.

REPORT DOCUMENTATION PAGE

Form Approved
OMB No 0704-0188

1. AGENCY USE ONLY (Leave blank)	2. REPORT DATE	3. REPORT TYPE AND DATES COVERED
	January 1993	Scientific No. 2

4. TITLE AND SUBTITLE
Handbook for the USAF Space Environment Standard (MIL-STD-1809)

5. FUNDING NUMBERS
Project Order GLHO-8048
PE: 63410F
PR 2821 TA 01 WU AE

6. AUTHOR(S)
Staff, Space Sciences Laboratory

7. PERFORMING ORGANIZATION NAME(S) AND ADDRESS(ES)
The Aerospace Corporation
El Segundo, CA 90245

8. PERFORMING ORGANIZATION REPORT NUMBER

9. SPONSORING/MONITORING AGENCY NAME(S) AND ADDRESS(ES)
Phillips Laboratory
29 Randolph Road
Hanscom AFB, Ma 01731-3010

Contract Manager: Allen Rubin/GPSP

10. SPONSORING/MONITORING AGENCY REPORT NUMBER
PL-TR-93-2010

11. SUPPLEMENTARY NOTES

12a. DISTRIBUTION/AVAILABILITY STATEMENT
Approved for public release; distribution unlimited

12b. DISTRIBUTION CODE

13. ABSTRACT (Maximum 200 words)

The Handbook for the Space Environment Standard (MIL-STD-1809) is a companion document to the Standard. The Standard is necessarily a very concise document, so that the Handbook is intended to make its usage easier. The Handbook describes the sources of the environmental models cited in the Standard, as well as the usage of the models, and their limitations. Means for obtaining the cited models are given as well. With the exception of the space debris model, the Handbook covers only the natural space environment. The Handbook provides a general overview of the various components of the space environment and the generally accepted understanding of them at the current time. A bibliography is provided to aid in understanding the materials presented in the Handbook and Standard.

14. SUBJECT TERMS
Space Environment Handbook
Natural Space Environment
Space Environment Models
MIL-STD-1809

15. NUMBER OF PAGES
70

16. PRICE CODE

17. SECURITY CLASSIFICATION Or REPORT	18. SECURITY CLASSIFICATION OF THIS PAGE	19. SECURITY CLASSIFICATION OF ABSTRACT	20. LIMITATION OF ABSTRACT
Unclassified	Unclassified	Unclassified	SAR

Table of Contents

HANDBOOK

for the

USAF SPACE ENVIRONMENT

STANDARD

(Mil-Std-1809)

Handbook for the

USAF SPACE ENVIRONMENT STANDARD

Forward:

This handbook is intended to be used in conjunction with MIL-STD-1809 (USAF). Its primary purposes are to indicate how the data listed in the Standard are to be used and to indicate the limits of usefulness of the Standard. It provides a general overview of the various components of the space environment and our understanding of them. It discusses the accuracy of models and methods recommended by the Standard. It provides some guidance to the use of models and methods. It attempts to provide uidelines to the use of the Standard, especially in the design of spacecraft and space systems, for which trade-offs in reliability, survivability, and capability are always required. This handbook should assist the user in evaluating the probable effects of various trade-offs in specifying the natural environment to which the spacecraft or space system is designed. Finally, it also provides a list of reference materials which may be of further help in understanding the material presented here and in the Standard.

In application of the Standard to a particular system or mission, the hazard of overdesign should be avoided. The vulnerability of individual sensors or subsystems may or may not equate to vulnerability of the system as a whole. The vulnerability of individual subsystems with respect to an environmental parameter may vary from no vulnerability at all to extreme sensitivity. The capability, reliability, and survivability of a system are determined by the characteristics of its subsystems. Therefore, designing a system to the environmental parameters set forth in the Standard means designing *subsystems* to these parameter values. The values of the various parameters supplied in the Standard are nominally severe limits. These are the values to be used unless designing to them would impose a significant cost or performance impact. In such a case, the system, orbit, and

mission should be analyzed to ascertain whether designing to a reduced environment would still provide adequate margin for successful performance of the mission. The rationale behind this approach is that, for short missions or particular orbits, the probable environment may be less severe than the environment specified in the Standard.

Anomalies and Significance of the Space Environment

Figure 1 is a cartoon showing the general relationship between the various regions of the geomagnetosphere and space environments which affect spacecraft within them. Space is not benign. It is quite hostile to systems placed in it. Surfaces suffer degradation from the effects of solar x-rays and ultraviolet radiation, impact from low energy protons and electrons, erosion by atomic oxygen at lower altitudes, impacts from micrometeoroids, enhanced contamination due to charging of the surfaces by plasmas, degradation from consequent microdischarges within the surface materials, and other effects. Sensor performance is degraded by energy deposition in sensitive detector elements by penetrating protons, electrons, and cosmic rays. Low-temperature elements such as long-wavelength IR systems can have a significant heat load imposed by the particle environment. Optical component performance is degraded by scintillation and Cerenkov radiation within the elements caused by high energy particles. Transmittance of optical materials is degraded by radiation-dose effects. Low power electronic chips that are geometrically small can suffer single event phenomena (SEP) such as upsets (logic state change, SEU), latch-up (logic states which can not be changed by normal on-chip signals), and burnout (in which the chip is permanently damaged). SEP are usually caused by heavy-element cosmic rays such as iron nuclei. Even the orbit of a low altitude spacecraft can be significantly perturbed by increases in the residual atmospheric density due to elevated solar EUV (Extreme Ultraviolet) emissions during intervals of solar activity. Variations in ionospheric density can have significant effects on

electromagnetic signal propagation. Other effects can also degrade the performance of a space system. While our knowledge of the environment is continuing to increase at a moderate rate, and thus may lead us to identify new hazards, it is the advance of technology (which provides increasingly sophisticated and thus increasingly vulnerable spacecraft hardware) that provides the primary impetus for the definition of new threats to space systems from the already known environment (e.g., SEU, dose effects, heating of cryogenic surfaces by particles). The following sections contain brief overviews of the various environmental constituents. For more extensive discussions, see the *Handbook of Geophysics and the Space Environment*, published by the Air Force Geophysics Laboratory (A. S. Jursa, Ed., 1985; NTIS Accession # AD-A167000).

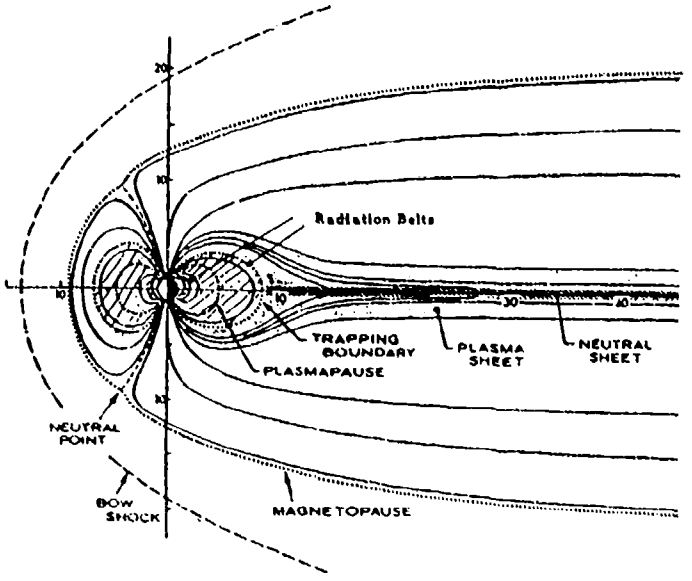

Figure 1. Configuration of the magnetosphere showing the radiation belts and the various plasma regimes (after Ref. 1.10).

1. Geomagnetic Field

1.1 Environment Overview

The geomagnetic field, **B**, is conveniently regarded as a superposition of internal, external, and induction fields. The internal field is regarded as arising from geomagnetic dynamo currents that flow in the Earth's core and (in principle) from crustal concentrations of magnetic material. The external field is regarded as arising from magnetospheric currents and (to a negligible extent) from the partial penetration of the magnetosphere by the solar-interplanetary magnetic field. The induction field results from currents that flow in the ionosphere and in the Earth in response to temporal variations in the magnetospheric currents.

The variations in the field due to these ionospheric currents, especially in the auroral region, can be troublesome to satellite operations, such as those which use magnetic torquing to dump stored angular momentum from attitude-control flywheels. Transient field variations during magnetic storms may result in apparent reversals of the field at geosynchronous altitudes (as when the field is compressed to the extent that the magnetopause moves past the geostationary satellite) severely affecting satellites which rely on the Earth's field for orientation control

The Internal Field

The magnetic field produced by geomagnetic dynamo currents is conventionally represented outside the core as the gradient of a scalar potential expanded in spherical harmonics of degree n and order $m \leq n \leq 10$. The corresponding Schmidt-normalized expansion coefficients (g_n^m, h_n^m) constitute a model known currently as the IGRF

(International Geomagnetic Reference Field) and retrospectively as the DGRF (Definitive Geomagnetic Reference Field) for the epoch of interest.

Tables of IGRF and DGRF coefficients are routinely published at five-year intervals. The most recent compilation (Ref. 1.1, IAGA Div. I, W. G. 1, 1986) provides coefficients (g_n^m,h_n^m) for the years 1945, 1950, 1955, . . . , 1985 to facilitate interpolation and time derivatives $(\dot{g}_n^m,\dot{h}_n^m)$ to facilitate extrapolation beyond 1985. Temporal variation of the expansion coefficients reflects what is called "secular variation" of the **B** field, a phenomenon that includes pole migration (~2 km/yr), diminution of the magnetic dipole moment (~0.09%/year), and other temporal variations that are more difficult to visualize. The DGRF and IGRF coefficients for Epoch 1985.0 are provided at the end of this section.

For some purposes it is sufficient to regard the internal field as approximately dipolar. The best-fitting dipole for Epoch 1989.0 has a moment $\mu \sim 0.305$ G-R_e^3 and is calculated from the IGRF coefficients $(g_n^m,h_n^m;\dot{g}_n^m,\dot{h}_n^m)$ with $0 \le m \le n \le 2$ to be located about 512 km from the geocenter and to be tilted by about 11° relative to the Earth's rotation axis. It is convenient in some applications to regard the geocenter as being displaced 512 km from the origin of the dipolar coordinate system (viz., 500 km from the dipole axis and 110 km south of the magnetic equator, see Figure 1.1). Each of the specified distances is presently increasing at a rate of about 2 km/yr. The offset-dipole model can largely account for the tendency of charged particles to precipitate into the atmosphere above the South Atlantic region with greater probability than elsewhere. Figure 1.2 depicts the surface field of the Earth and clearly shows the low-field region referred to as the "South-Atlantic Anomaly", or SAA. True magnetic anomalies (i.e., deviations from the best-fitting dipolar **B** field) are optimally represented (Refs. 1.2, 1.3) by transforming to offset dipole coordinates and identifying any nonvanishing expansion coefficients (G_n^m,H_n^m)

that remain for $n \geq 2$ in this representation. Spherical harmonics of degree $n \leq 10$, however, can at best resolve continent-sized ($\sim 2.5 \times 10^7$ km^2) magnetic anomalies. There is circumstantial evidence (Ref. 1.4) from the "spectrum" of spherical-harmonic expansion coefficients ($m \leq n \leq 25$) obtained via MAGSAT data that anomalies describable by harmonics with $n \leq 12$ probably originate in the core (dynamo) region, whereas anomalies describable by harmonics with $n \geq 14$ probably originate in the crust from local concentrations of magnetic material.

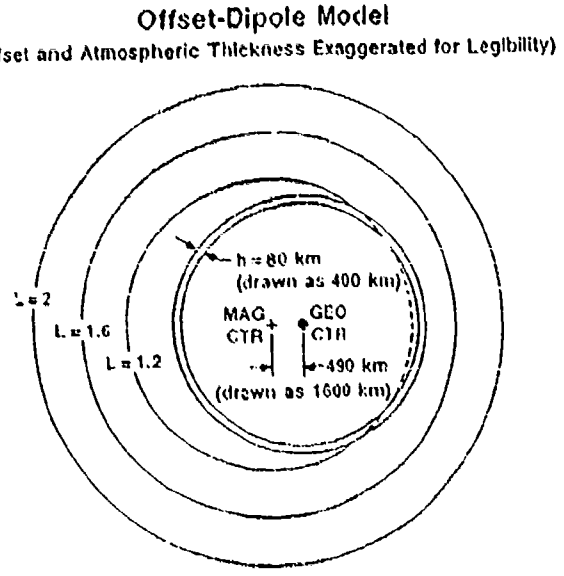

Figure 1.1 Cartoon depicting the offset dipolar nature of the geomagnetic field.

Figure 1.2 Contour plot of the surface geomagnetic field.

The External Field

The external field is that portion of the field which is produced by magnetopause currents, tail currents, ring currents, and Birkeland currents. The **B** field produced by magnetopause and tail currents can be approximated by the source-surface model of the magnetosphere (Ref 1.5) which provides a set of spherical-harmonic expansion coefficients g_n^m for the scalar potential from which this **B** can be derived at any point in the magnetosphere sunward of the tail. The tail field itself is not derivable from a scalar potential in this model, but it is derivable from a geometrical construction that maps field lines into the tail from a cross-magnetospheric surface (Fig. 1.3) that marks the outer limit of validity of the spherical-harmonic expansion. Schulz and McNab (Ref 1.8) have obtained simple trigonometric expressions for the expansion coefficients g_n^m as functions of the angle ψ between the internal dipole (about which the expansion is centered) and the solar-wind velocity (to which the axis of symmetry of the magnetopause in this model is parallel).

The universal scale for distances in the source-surface model is b, the distance from the point dipole to the subsolar point on the magnetopause, as measured along the axis of symmetry of the magnetopause. The value of b adjusts itself so as to achieve pressure balance between the solar wind and the magnetospheric **B** field. The pressure of the solar wind at the nose of the magnetosphere is $\Sigma_i N_i m_i u_i^2$ in a hydrodynamic-flow model and twice as much in a specular-reflection model, where N_i, m_i, and u_i denote (respectively) the upstream number density, ionic mass, and upstream flow velocity of species i. The symbol Σ_i denotes a summation over ionic species. The balancing pressure $B^2/8\pi$ at the nose of the magnetosphere is obtainable from the source-surface model and (other things being equal) is proportional to b^{-6}. Thus, the value of b is inversely proportional to the sixth-root of the solar wind pressure. Magnetopause

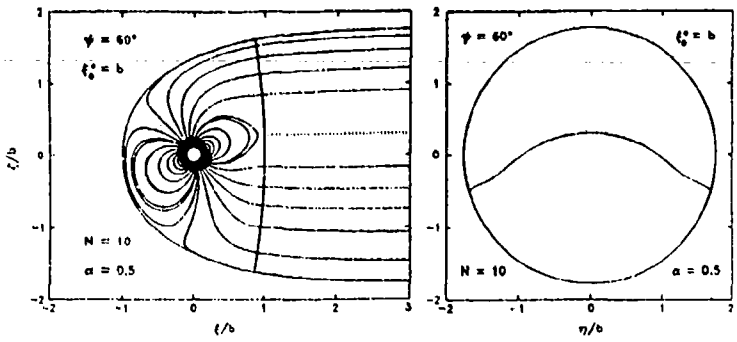

Figure 1.3. Left Panel: Representative field lines (Ref. 1.8) in the meridional plane that contains the tail axis ($\rho = 0$) and the magnetic dipole axis. Coordinate ζ is measured from the plane that perpendicularly intersects this meridional plane along the tail axis. Selected field lines emanate from the planetary surface ($r = 1\ R_e = b/10$) at 5° intervals of magnetic latitude (viz., 90°, 85°, 80°, , ,) for angle $\psi = 60°$ between dipole moment and solar-wind velocity. Right panel: Intersection of neutral sheet with the plane $\zeta = +\text{inf}$ for $\psi = 60°$. Coordinate η is measured from the plane of symmetry in which the field lines plotted in the left panel lie.

currents have the effect of "compressing" the dipolar **B** field, especially on the day side. Tail currents have the effect of distending the dipolar **B** field, especially on the night side. The net effect at the Earth's surface for ψ=90° is an augmentation $(\Delta \mathbf{B})_m \sim [12.73(10\ R_e/b)^3 - 2.75(10R_e/b)^4 \cos\phi]$ nT to the (northward) equatorial magnetic field that the Earth's dipole provides at low latitudes. The magnetic longitude ϕ in this approximate expression for $(\Delta \mathbf{B})_m$ is measured from the midnight meridian, and a nominal value of b is about 10 R_e on average. The foregoing expression for $(\Delta \mathbf{B})_m$ is deduced from the source-surface model of the magnetosphere (Ref. 1.5). Other magnetospheric models

yield qualitatively similar results.

Actual measurements of B at the Earth's surface suggest that the equatorial augmentation $(\Delta B)_m$ produced by magnetopause currents is more than offset by an equatorial reduction $(\Delta B)_r$ produced by the ring current, which consists of hot plasma governed by the laws of adiabatic charged particle motion in the interior of the magnetosphere. A representative model for the radial profile of $(\Delta B)_r$ at low latitudes is illustrated in Figure 1.4. The total azimuthal current borne by ring-current particles is proportional to their total kinetic energy, which thus can be monitored by measuring the equatorial value of $(\Delta B)_r$ at the Earth's surface. The geomagnetic index D_{st} (Ref. 1.6) serves as a measure of these physical quantities. The D_{st} index is measured at hourly intervals by averaging the deviations ΔH in the horizontal component of **B** at several low-latitude stations (well distributed in longitude) from the nominal (quiescent) values of the horizontal component of **B** at these stations. It is presumed, however, that measured D_{st} consists of $(\Delta B)_r$ and of the corresponding induction field, evaluated at the Earth's surface. The induction field (see below) might be as much as half as large as $(\Delta B)_r$ there, in which case.(cf. Figure 1.3) D_{st} would be equal to (3/2) $(\Delta B)_r$ at the Earth's surface.

Birkeland currents flow parallel to **B** along auroral and slightly sub-auroral field lines. They are largely a consequence of the large scale "convection" electric field $\mathbf{E}_c$ which (except on the auroral oval and its extension to the boundary of the magnetosphere) is directed perpendicular to **B**. A fairly realistic model (Ref. 1.7) yields $\mathbf{E}_c = -\text{grad}[b\mathbf{E}_c(3L^*/L)^{1/2} \sin \phi]$ for $L > L^*$ (i.e., on polar-cap field lines) and $\mathbf{E}_c = -\text{grad}[\text{sqrt}(3)b\mathbf{E}_c(L/L^*)^2 \sin \varphi]$ for $L < L^*$ (i.e., on sub-auroral field lines). This model is consistent with a uniform electric field $\mathbf{E}_c = -y\mathbf{E}_c$ across the distant tail of the magnetosphere. At ionospheric altitudes the electric field $\mathbf{E}_c$ is found to point away from the auroral oval ($L = L^*$) for $\sin\phi > 0$ (i.e., in the morning sector of local time) and toward

the auroral oval for $\sin\phi < 0$ (i.e., in the evening sector). Current continuity at $L = L^*$ thus requires a downward Birkeland current in the morning sector and an upward Birkeland current in the evening sector. These constitute the so-called Region-I current system, which is connected to the magnetopause and cross-tail currents. The boundary conditions of the problem permit a component of **E** parallel to **B** at L L*, and there seems indeed to be a potential drop of several kilovolts along **B** in an auroral arc that is located in the evening sector of local time. It is this potential drop that accelerates auroral arc electrons just before they precipitate into the upper atmosphere, and it is this potential drop that accelerates the upward field-aligned ion beams that are characteristic of this sector of the auroral oval.

The Region-I Birkeland current is largely balanced by a return current, known as the Region-II Birkeland current, which is a response to the requirement of ionospheric current continuity at L<L*. where the meridional component of $\mathbf{E}_c$ in the Volland model (Ref. 1.7) is given by $\theta\ \mathbf{E}_c \sim \mathrm{sqrt}(3)\ b\ \mathbf{E}_c\ (2/L^*)^2\ \csc^5\theta\ \sin\phi$ and thus shows a strong dependence on magnetic latitude $(\pi/2-\theta)$. It has been estimated (Ref. 1.11) that about 80% of the Region-I current returns to the magnetosphere as Region-II current, so that only about 20% flows across the noon-midnight meridional plane in the ionosphere. This means that the magnetic signature of the Birkeland system is quite important in and near the auroral oval but greatly attenuated (from what it would have been in the absence of Region-II currents) at other L values. The Region-II current system closes via the plasma sheet and ring current in the magnetosphere and via the Region-I system in the ionosphere. Models of the magnetic signature of the Birkeland current system are mostly schematic rather than quantitative, but fortunately, the magnetic effects are mostly local rather than global. The magnetospheric electric fields that drive ionospheric currents are more or less variable in time, and the variability of the resulting magnetic signatures (as observed at ground stations) can serve as an indicator of magnetospheric activity. The

various indices in common use are described in great detail in Ref. 1.6. One that merits particular mention here is the K_p index, which is the average of a quasi-logarithmic measure of the amplitude of variation of the magnetic signals observed at a dozen high latitude (48° to 63° geomagnetic) stations during each 3-hr time interval. The K_p index is conceived as being continuously variable over the interval $0 \leq K_p \leq 9$ but is usually rounded to the nearest third of a integer, the result being quoted as 0o, 0+, 1-, 10, 1+, . . . , 8+, 9-,9o. These correspond to disturbance values ranging from 0 to 400 nT. The a_p index is a linear version of K_p. The daily average of a_p is designated A_p. The AE (Auroral Electrojet) index is a measure of the azimuthal ionospheric current that connects the downward (morning sector) Region-I Birkeland current with its upward (evening sector) counterpart. The D_{st} index, described above, is a low-latitude measure of the magnetic field produced by the ring current. The D_{st} index is a continuous variable (usually negative, because the ring current produces a southward field perturbation at low-latitude ground stations) that can attain a value as extreme a -200 nT or even -300 nT during a major storm or a value as moderate as $\pm$ 25 nT (positive values arising from the symmetric part of the magnetopause current) during extremely quiet intervals.

Induction Effects

Any ground-based measurement of the magnetic signature of a magnetospheric or ionospheric current system is potentially contaminated by currents induced to flow in the Earth by the temporal variations of such external currents. A simple model for Earth induction can be constructed by supposing that an externally imposed magnetic-field perturbation of frequency $\omega/2\pi$ is excluded from a sphere of radius $R_c(\omega) < R_e$, where R_c is (by virtue of skin-depth considerations) a monotonically increasing function of ω. Thus, for example, the application of an asymptotically uniform field $B_z(\omega)$ results in the induction of a dipole moment such that the total field perturbation is given by $\Delta \mathbf{B} = B_z$

grad[R cos θ + ($R_c^3/2R^2$) cos θ] at geocentric distances R > R_c. The equatorial field perturbation is thus [1+($R_c^3/2R^2$)]$B_z(\omega)$ at arbitrary R and [1+($R_c^3/2R_e^2$)]$B_z(\omega)$ at the Earth's surface. More generally, if the B field produced by external currents is expressed in the form $\mathbf{B}^{ext} = \Sigma_n^m R_e\ grad\ [(R/R_e)^n\ (g_n^m \cos m\phi + h_n^m \sin m\phi)\ P_n^m(\theta)]$ in some annular volume immediately surrounding the Earth, the induction field in that same annular volume would be given by $\mathbf{B}^{ind} = \Sigma_n^m Rc\ grad\ [n(n-1)^{-1}\ (R_c/R_e)^{2n}\ (g_n^m \cos m\phi + h_n^m \sin m\phi)\ P_n^m(\theta)]$ where $P_n^m(\theta)$] is the associated Legendre function and Σ_n^m denotes the double summation over m and n such that $0 \leq m \leq n$. Of course, the expansion coefficients g_n^m and h_n^m pertain to a particular frequency $\omega/2\pi$ in the Fourier decomposition of the externally applied **B** field, and the inductive response to an applied field of arbitrary time dependence can be reconstructed by superposition.

There is a further induction effect that needs to be considered in magnetospheric modeling, and this is the modification of the magnetopause current by the presence of other magnetospheric currents. The ring current, for example, effectively constitutes an additional dipole moment, which must be added to the Earth's moment (and diminished by the induced moment) when computing the value of b for a given solar-wind pressure. However, because the effective radius of the ring current is typically a large fraction of b itself, the octupolar component of the ring-current field is not negligible at the magnetopause, and this means that a new set of coefficients (g_n^m) must be computed from the source-surface model (Refs.1.5, 1.8) to describe the B field that results from the magnetopause and tail currents. Moreover, the day-night asymmetry of the magnetospheric **B** field makes it unlikely that the ring current itself will be axisymmetric in reality, although simple models (e.g., the one illustrated in Figure 1.4) have traditionally treated it as such.

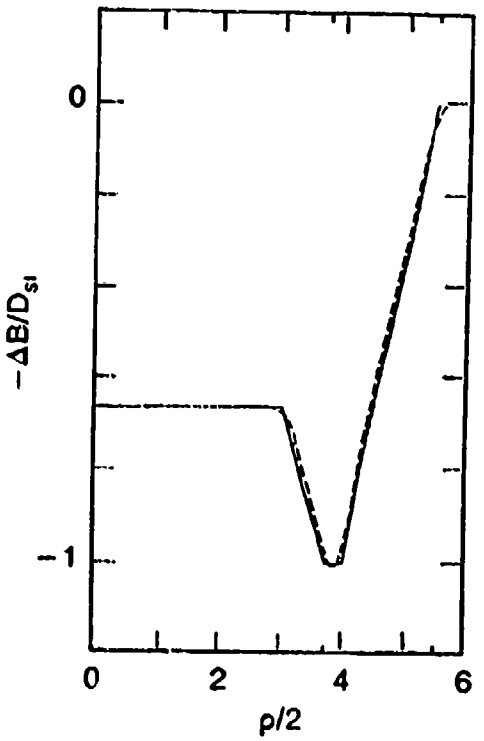

Figure 1.4 Model for equatorial B-field perturbation (dashed curve) produced directly by ring current (Ref. 1.9) and piecewise-linear approximation thereof (solid "curve"). Coordinate ρ here represents distance from dipole axis.

Other Coordinate Systems

For some purposes, the use of special coordinate systems either simplifies calculations or concepts, or reduces the number of variables in a system. The definitions of several of these coordinate systems are presented below for informational purposes. These coordinate systems, all of which are Earth-centered, are the following:

a) Ecliptic Coordinates

In this system, X points sunward, Z points northward perpendicular to the ecliptic plane, and Y completes a right-handed orthogonal set.

b) Solar Magnetospheric Coordinates

In this system, X again points sunward, Z points northward in the plane formed by the X-axis and the dipole axis, and Y again completes a right-handed orthogonal set.

c) Solar Magnetic Coordinates

In this system, Z points northward along the dipole axis, X is perpendicular to Z in the plane formed by the dipole axis and the Earth-Sun line, and Y again completes a right-hand orthogonal set.

A detailed discussion of these coordinate systems may be found in Ref. 1.12.

1.3 Models

A number of external field models and field-line codes are listed in Ref. 1.13. The primary models in use in magnetospheric physics are the Tsyganenko (Ref 1.14) and Olsen--Pfitzer (Ref. 1.15) models. These models are updated as new understanding of the magnetosphere is achieved. Use of these models should be coordinated with their authors.

1.4 References

1.1 IAGA Division I, Working Group 1, International Geomagnetic reference field revision 1985, *Eos, Trans. Am. Geophys. Union* , *67* , 523-524, 1986

1.2 Bernard, J., J. Cl. Kosik, G. Laval, R. Pellat, and J.-P. Philippon, Representation optimale du potentiel geomagnetique dans le repere d'un dipole decentre incline, *Ann. Geophys* ., *25* , 659-666, 1969

1.3 Hilton, H. H., and M. Schulz, Geomagnetic potential in offset-dipole coordinates, *J. Geophys. Res.* , *78* , 2324-2330,1973.

1.4 Langel, R., A. , and R. H. Estes, A geomagnetic field spectrum, *Geophys. Res. Lett* ., *9* , 250-253, 1982.

1.5 Schulz, M. and M. C. McNab, Source surface model of the magnetosphere, *Geophys. Res. Lett* ., *14* , 182-185, 1987.

1.6 Mayaud, P. N., *Derivation, Meaning, and Use of Geomagnetic Indices* , 154 pp., Geophys. Monogr. 22, Am. Geophys. Union, Washington, D. C. 1980.

1.7 Volland, H., Models of global electric fields within the magnetosphere, *Ann. Geophys* ., *31* , 159-173, 1975.

1.8 Schulz, M. and M. C. McNab, Source surface model of a planetary magnetosphere, *J. Geophys. Res* ., *97* , to be published, 1992.

1.9 Söraas, F., and L. R. Davis, Temporal variations of the 100 keV to 1700 keV trapped protons observed on satellite Explorer 26 during first half of 1965, *NASA/GSFC Rept* . *X-612-68-328* , Goddard Space Flight Center, Greenbelt, MD, 1968.

1.10 Handbook of Geophysics and the Space Environment, Air Force Geophysics Laboratory, A. S. Jursa, Ed., 1985. NTIS ADA 167000.

1.11 Iijima, T., and T. A. Potemra, The Amplitude Distribution of Field-aligned Currents at Northern High Latitudes Observed by TRIAD, *J. Geophys. Res.* , *81* , 2165-2174, 1976.

1.12 Russell, C. T., Geophysical Coordinate Transformations, *Cosmic Electrodyn.* , *2* , 184-196, 1971.

1.13 Bilitza, D., Solar-Terrestrial Models and Application Software, *NSSDC/WDC-A-R&S 90-19*, National Space Science Data Center, Goddard, MD, July 1990.

1.14 Tsyganenko, A Magnetospheric Magnetic Field Model with a Wrapped Tail Current Sheet, *Planet. Space Sci.* 37, 5-20, 1989.

1.15 Olsen, W. P., and K. A. Pfitzer, A quantitative Model of the Magnetospheric Magnetic Field, *J. Geophys. Res.*, 79, 3739, 1974.

2. Neutral Atmosphere

2.1 Overview

The neutral atmosphere above 100 km experiences diurnal, seasonal, and solar cycle variations in density, temperature, and velocity. The primary causes of these variations are solar UV energy input and solar tides (which produce subsolar upwelling), lunar tides, and energy deposition in the polar region from auroral processes. These effects complicate the prediction of accurate ephemerides for low altitude satellites. A thorough discussion of these effects is beyond the scope of this handbook.

An additional concern associated with the neutral atmosphere is the presence of atomic oxygen, which is produced from molecular oxygen by the Sun. At low altitude orbital velocities, the effective kinetic energy of an oxygen atom relative to surface of a satellite is about 5 eV. This kinetic energy drives chemical reactions on the satellite surface, producing oxides. Volatile oxides evaporate, removing material and chemical constituents from surface materials. This atomic-oxygen-driven chemical erosion can have serious consequences on most low altitude satellites. The design of low altitude satellites must include this environment as a driving factor.

2.2 Models: Use and Utility

The values of density, composition, and temperature shown in the figures in Section 3.3 of the Standard are representative of the equatorial thermosphere at times of low magnetic activity. Variations from this condition described in the text allow an extrapolation to be made from the figures for a variety of other latitudes, times and conditions. During exceptional magnetic or solar activity, thermospheric variability may be several times greater than the values discussed in the text. The numbers presented

there should be used only as a guide for first order approximations. If the density, composition or temperature prescribed according to Section 3.3 are within a factor of 2 of system-design limitation, more detailed calculations using the MSIS-86 or MSIS-83 thermosphere model (Refs. 2.1, 2.1a,2.2) should be performed. Of particular importance in this regard is density: Small errors in density specification can cause large errors in orbital lifetime calculations.

The density, composition, and temperature values presented in Section 3.3 are based on the MSIS-86 thermosphere model (Ref. 2.1), an empirical model based on a large collection of ground, spacecraft, and rocket data. User-provided input of day, time, altitude, latitude, longitude, local solar time, magnetic index (Ap), averages of 10.7 cm radio flux over the past three solar rotations, and the previous day's 10.7 cm flux produce an output of composition, density and temperature. Detailed evaluations of the MSIS-86 model show a typical error (standard deviation of about 15%). A previous version of this model, MSIS-83 (Ref. 2.2) may be used alternatively for detailed calculations. While MSIS-86 is slightly better than MSIS-83 overall, the former underestimates variability at high latitudes during intervals of low solar activity. Investigators should use MSIS-83 under these conditions.

The discussion of thermospheric winds in Section 3.3 is based both on observation and theoretical models of thermosphere dynamics. The numbers can be used only for systems analysis in the most general way, since thermospheric winds are highly variable in magnitude and direction. The values offered in Section 3.3 should be considered only a guide for estimating order-of-magnitude effects. Detailed models of thermospheric dynamics (Refs. 2.3, 2.4) discuss the full range of thermospheric wind variability. Other references for average wind conditions (Ref. 2.6) and gravity wave density amplitudes (Ref. 2.7) are also listed.

The MSIS-86 model is available from NSSDC on their NODIS account (NTS-DECNet node NSSDCA). The software available on NODIS includes the model as a FORTRAN subroutine package, a driver program, and a test program. This software is also available as an interactive program on EnviroNET, which is on the ENVNET node at GSFC.

2.3 References

2.1 Hedin, A. E., MSIS-86 Thermospheric Model, J. Geophys. Res., 92, 4649-4662, 1987.
2.1a Hedin, A. E., Extension of the MSIS Thermosphere Model into the Middle and Lower Atmosphere, J. Geop[hysical Research, 96, 1159-1172, 1991

2.2 Hedin, A. E., A Revised Thermospheric Model Based on Mass Spectrometer and Incoherent Scatter Data: MSIS-83, J. Geophys. Res., 88, 10170-10188, 1983.

2.3 Forbes, J. M., Middle Atmosphere Tides, J. Atmos. Terr. Phys., 46, 1049-1067, 1984.

2.4 Smith, R. W., D. Rees, and R. D. Stewart, Southern Hemisphere Thermosphere Dynamics, Rev. Geophys., 26, 591-622, 1988.

2.5. Guide to Reference and Standard Atmospheres, ANSI/AIAA G-003-1990; American Institute of Aeronautics and Astronautics, 370 L'Enfant Promenade, S.W., Washington, D.C. 20024-2518

2.6 Hedin, A., E., M.A. Biondi, R.G. Burnside, G. Hernandez, R.M. Johnson, T.L. Killeen, C. Mazaudier, J.W. Meriwether, J.E. Salah, R.J. Sica, R.W. Smith, N.W. Spencer, V. B. Wickwar, and T.S. Virdi, J. Geophys. Res. 96, 7657-7688, 1991

2.7 Hedin, A. E., and H. G. Mayr, Characteristics of Wavelike Fluctuations in Dynamics Explorer Neutral Composition Data, J. Geophys. Res., 92, 11159-11172, 1987.

3. Plasma Environment: Ionosphere

3.1 Overview

The characteristics of the ionosphere are of importance to space systems primarily because of the effects of the ionosphere on signal propagation. Various ionospheric effects such as refraction, dispersion, absorption, Faraday rotation, and scintillation can degrade system performance. Some concern has been raised also about the possibility of surface charging in the auroral zone, where large fluxes of thermal and suprathermal electrons and ions are encountered. Surface charging can occur because of the large difference in mobility between the electrons and ions that constitute the ionospheric plasma (Refs. 3.6 and 3.7). Thermal protons have a speed which is of the same order as that of a space vehicle. In the wake of a large orbiting object, thermal protons have a reduced accessibility because the object is traveling faster than many of the ions. Electrons have unimpeded access to vehicle surfaces, even in the wake, because thermal electron speeds are large compared to the speed of an orbiting vehicle. The difference in accessibility produces a difference in charging currents, and this ultimately produces a negative potential on wake surfaces which are shadowed. Surfaces which are sunlit have sufficiently large photo-emission currents to produce a slightly positive potential under all conditions. Of course, this also means the vehicle frame develops a slightly positive charge. The combination of sunlit structure and shadowed wake areas which are insulated from the structure will result in potential differences which may produce deleterious effects on components and systems.

Above 2000 km, the ion density falls gradually with increasing altitude until, typically at equatorial altitudes of 3 to 3.5 R_e (L = 4 to 4.5), a more abrupt decrease in ion density occurs (typically of 1.5 to 2 orders of magnitude in $\Delta L \sim 0.1$ to 0.2). This abrupt decrease

is known as the plasmapause and the region enclosed by it is known as the plasmasphere. Typical densities outside the plasmasphere are of the order of 0.1-1/cm^3. The density discontinuity (plasmapause) at a given longitude roughly follows the geomagnetic field line to higher latitudes. Any spatial variation in plasma density can affect the propagation of radio waves. Moreover, the steep gradient in density across the plasmapause can act as a one-sided duct for low frequency waves.

3.2 Models

At high latitudes, in the auroral and polar-cap regions, scintillation can be severe during solar maximum. The Air Weather Service operates a scintillation model, WBMOD, based on data obtained from the DNA Wideband satellite. This model provides phase and amplitude scintillation indices at any geographic location on a specified day and time, for a given sunspot number and magnetic activity. A real-time updated WBMOD is being developed which can be driven with data from the network of GPS observing stations as well as from irregularity sensors on the DMSP satellites. Commonly available models and their availability are:

International Reference Ionosphere

This model is sanctioned by the Committee on Space Research (COSPAR) and the International Union of Radio Science (URSI). Working groups from these organizations update it periodically as new data become available. It is a REFERENCE model. Its purpose is to serve as a standard against which new data can be compared. It DOES NOT serve as a useful operational model. IRI describes electron and ion densities and temperatures and ion composition from about 50 km to 2000 km. Updated copies of the software which calculate values from the current model are available from the National Space Science Data Center, COSPAR/URSI Working Group on IRI, NASA/GSFC, Code

933, Greenbelt, MD 20771. It is also available on the NTS-DECNet node NSSDCA in the NODIS account.

Bent Model

This model, based on topside ionograms from Alouette, in-situ data from Ariel, bottomside ionograms, and the CCIR maps for the F2 peak, describes the ionospheric electron density as a function of geographic location, time, and solar $F_{10.7}$ flux. It is used widely for ionospheric refraction corrections. A comparison between it and IRI is given in Ref. 3.19. The model is described in Ref 3.11.

FAIM Model

This is the Fully Analytical Ionospheric Model (Ref. 3.12) which traces its history through several previous models (Refs. 3.13, 3.4), originating in the Chapman functions for the E, F1, and F2 layers. All of these models are valid at low latitudes only. The FAIM model, which has been extended in validity to the equatorial region, is available from D. N. Anderson on NTS-DECNet at AFGL::DANDERSON as a Fortran program.

Other Models

Several other useful models exist which are regional or global models (usually theoretical) which have distinct advantages and disadvantages for specific applications (e.g., Refs. 3.15, 3.16). For a specific application in which the IRI model indicates that the ionosphere may have a significant effect, one of these other models should be used. If available to the user, the AWS ICED (WBMPD?) model (suitable updated with measured values of the effective sunspot number and auroral index) is recommended. If reduced accuracy is acceptable, the FAIM model is recommended. Again, we emphasize that IRI is a REFERENCE model for comparison purposes only.

3.3 References

3.1 Rawer, K., International Reference Ionosphere--IRI-79, Ed. J. V. Lincoln and R. O. Conkright, WDC-A-STP, NOAA, Boulder, CO, 1981.

3.2 Rawer, K., International Reference Ionosphere, Adv. Space Res., 2, No. 10, 181-257, 1982.

3.3 Hardy, D. A., M. S. Gussenhoven, and E. Holman, A Statistical Model of the Auroral Electron Precipitation, J. Geophys. Res. 90, 4229, 1985.

3.4 Dana, R. A., and D. L. Knapp, The Impact of Strong Scintillation on Space Based Radar Design II: Noncoherent Detection, IEEE Trans. Aerospace and Electronic Systems, AES-22, 34-46, 1986.

3.5 Fremouw, E. J., and R. E. Robins, An Equatorial Scintillation Model, DNS TR-85-333, September 1985.

3.6 Gussenhoven, M. S., D. A. Hardy, F. Rich, W. J. Burke, and H.-C. Yeh, High Level Spacecraft Charging in the Low-Altitude Polar Auroral Environment, J. Geophys. Res., 90, 11009, 1985.

3.7 Yeh, H. -C., and M. S. Gussenhoven, The Statistical Electron Environment for DMSP Eclipse Charging, J. Geophys. Res., 92, 7705, 1987.

3.8 McNeil et al,

3.10 Bilitza, D. K. Rawer, and S. Pallaschke, Study of Ionospheric Models for Satellite Orbit Determination, Radio Sci., 23, 223, 1988.

3.11 Llewellen, S. K., and R. B. Bent, Documentation and Description of the Bent Ionospheric Model, AFGL Report AFCRL-TR-73-0657, Hanscom AFB, MA, 1973. (NTIS Accession # AD-772733)

3.12 Anderson, D. N., J. M. Forbes, and M. Codrescu, A Fully Analytical, Low- and Middle-Latitude Ionospheric Model, J. Geophys. Res., 94, 1520, 1989.

3.13 D. N. Anderson, M. Mendillo, and B. Herniter, A Semi-Empirical, Low-Latitude Ionospheric Model, Radio Sci., 22, 292, 1987.

3.14 Chiu, Y. T., An Improved Phenomenological Model of Ionospheric Density, J Atmos. terr. Phys, 37, 1563, 1975.

3.15 Sojka, J. J., and R. W. Schunk, Theoretical Study of the Seasonal Behaviour of the Global Ionosphere at Solar Maximum, J. Geophys. Res., 94, 6739, 1989.

3.16 CCIR Atlas of Ionospheric Characteristics, Comite Consultatif International des Radiocomunications, Report 340-4, International Telecommunications Union, Geneva, 1967 (Included in the IRI model available from NSSDCA::NODIS.)

4. Energetic Charged Particles

4.0 Overview

The space particle environment can be categorized by particle type, energy range, and origin. The particles of primary interest are magnetospherically-trapped protons and electrons, solar flare protons, and cosmic rays. Each of these main categories provides a particular environment that impacts the operation and performance of space systems. Moreover, the various regions of space can be characterized by the most important type of particle encountered there. For this overview, we will organize the discussion by region, starting from the from the top of the atmosphere and proceeding radially outward.

To one who is interested in ionizing particles in space, the top of the atmosphere can be regarded as being coincident with an altitude of 100 km. At this altitude (or within several kilometers of it), electrons and protons are quite effectively absorbed: any that mirror at or below this altitude are down into the even denser atmosphere and thus lost from the distribution. Their energy is deposited in the upper atmosphere. If a satellite at nominal altitude, (e.g.,1000 km over the equator) measures the pitch-angle distribution (defined with respect to the local magnetic-field direction) of energetic charged particles, it will see a maximum in the particle flux when looking perpendicular to the local field line and essentially no flux when looking along the field line. Any particles that would mirror below the top of the atmosphere, according to the adiabatic theory of charged-particle motion, are said to be in the local "loss-cone" and are largely absent from the pitch-angle distribution.. A further discussion of electron motion in the geomagnetic field is given in Section 4.2.1.

The energetic charged particles present just above the atmosphere are primarily electrons

and protons. Other energetic ions (E~10-60 keV) are well represented in the equatorial "ring current" region; other ions having very low energies (<10 eV) are well represented at low altitudes as part of the residual ionospheric plasma (see Section 2). These produce their own effects on space systems, but in this section we consider only the higher energy particles.

From the top of the atmosphere up to an equatorial altitude of about 1 R_e (Earth radius, =6371.2 km) resides the inner radiation belt. in which there are large fluxes of electrons with energies up to about 2 MeV and of protons with energies up to about 400 MeV. These are not cutoff energies above which there are no particles; they are energies above which so few particles are present that they are of no concern to most space systems.

As one continues upward toward equatorial geosynchronous altitude, large fluxes of lower-energy protons and an intense 'outer' belt of very energetic electrons are encountered. Beyond geosynchronous altitude, the energy of the typical trapped particle drops rapidly, as does the flux intensity, down to a thermal plasma regime (~1-10 keV temperature). However, as one goes up in altitude, the effectiveness of the geomagnetic shield decreases, and so lower-rigidity cosmic rays are also present (see Section 4.1). Energetic solar flare protons are encountered sporadically at geosynchronous altitude (see Section 4.3).

4.1 Cosmic Rays

4.1.1 Overview

Galactic cosmic rays come from outside the solar system and have energies ranging up to many GeV/nucleon. These are relatively few in number and affect sensors and subsystems mainly by producing spurious signals (backgrounds in sensors, false

commands) and SEP (Single Event Phenomena) such as SEU (Single Event Upsets, events in which the state of a logic device is changed), latch-up (in which a circuit is set into a permanent mode that can be changed only by removing power from the circuit), and burnout (in which irreversible damage is done to a circuit or component).

Solar Cycle Modulation

Galactic cosmic rays entering the solar system are scattered by irregularities in the interplanetary magnetic field (which is embedded in the solar wind), and it is believed that the particles have to diffuse through this medium in order to reach the Earth. During solar minimum the average activity of the Sun is diminished and the interplanetary medium is somewhat more orderly than during solar maximum. The result is a modulation ~40% in intensity for galactic cosmic rays at energies below ~1 Gev/nucleon. This modulation is anti-correlated with the solar activity cycle.

Magnetospheric Access

The geomagnetic field alters the trajectory of any charged particle traveling through it. Particles can either become trapped in, or excluded from, various parts of the magnetosphere, the locations of exclusion (which are relevant mainly for solar energetic particles and galactic cosmic rays) being determined by the energy, charge/mass ratio, and initial entry location and direction of the particle velocity. The energy, mass, and charge determine the magnetic rigidity of a particle, which is defined as the scalar momentum per unit charge. The rigidity and local pitch-angle determine the radius of curvature of the charged particle's trajectory in a magnetic field. Relatively low-energy ($\geq$ 10 MeV) protons can penetrate to geosynchronous altitudes from the outside. Satellites in geosynchronous orbit encounter essentially the same cosmic ray flux (E$\geq$ 100 MeV)

as would a probe in interplanetary space. Since geomagnetic field lines emanating from the polar caps are open, even very low-energy particles ($E \sim 10$ eV electrons, for example) can reach satellites in low polar orbits. In regions of the magnetosphere where there are trapped particles, however, low-rigidity cosmic rays are excluded and high rigidity cosmic rays are limited to specific access directions. The calculation of the corresponding particle trajectories for other than an idealized (dipolar) B field must be made numerically by selecting directions/rigidities as input. Then a time-reversed trajectory trace in a model magnetic field geometry can generate numerical estimates of cosmic ray cutoffs, but so far the numerical results are not entirely consistent with observational data. For this reason, the Standard does not address the question of energetic-particle access. Ref. 4.1.5, used by the CREME software (see below), offers such an approach, however.

4.1.2 Regions of Validity of the Standard

The cosmic ray flux recommendations presented in Mil Std 1802 have been generated from summaries of many years of observational data and will not change radically in the future. However, the CRRES satellite, launched in July 1990, has a large-geometric-factor cosmic-ray telescope which is making energy and mass-composition measurements of cosmic rays over a wide dynamic range. The orbit permits the measurement of cosmic ray fluxes near the equator from 350 km altitude out to near the geosynchronous orbit-region. When sufficient data have been accumulated and analyzed, this data set should provide the basis for better empirical modeling of cosmic ray access to the inner magnetosphere at low latitudes. For now, Ref. 4.1.5 may be used to determine such access.

4.1.3 Models: Use and Utility

The CREME (Cosmic Ray Effects on Microelectronics) software generates an empirical

model for the cosmic-ray energy flux or LET (Linear Energy Transfer) flux for an orbit by using the tabulated geomagnetic cutoff values from Ref. 4.1.5. The software includes the galactic cosmic ray spectrum. Solar proton fluxes are included as an option. Tables of microelectronics LET thresholds then permit an estimate of upset (SEU) rates. The software package is available from the National Geophysical Data Center, E/GC2, 325 Broadway, Boulder, CO 80303 (303-497-6346). For discussions of solar cosmic ray models, see Section 4.3.

4.1.4 References

4.1.1 Adams, J. H. Jr., R. Silverberg, and C. H. Tsao, Cosmic Ray Effects on Microelectronics, Part I: The Near-Earth Particle Environment , NRL Memorandum Report 4506, 1981. (NTIS Accession No. AD-A103897)

4.1.2 Adams, J. H., Jr., J. R. Letaw, and D. F. Smart, Cosmic Ray Effects on Microelectronics, Part II: The Geomagnetic Cutoff Effects , NRL Memorandum Report 5099, 1983. (NTIS Accession No. AD-A128601)

4.1.3 C. H. Tsao, R. Silberberg, J. H. Adams, Jr., and J. R. Letaw, Cosmic Ray Effects on Microelectronics, Part III: Propagation of Cosmic Rays in the Atmosphere, NRL Memorandum Report 5402, 1984 (NTIS Accession No. AD-A145026)

4.1.4 Adams, J. H., Jr., Cosmic Ray Effects on Microelectronics, Part IV , NRL Memorandum Report 5901, 1986.

4.1.5 Shea, M. E., and D. F. Smart, Tables of Asymtotic Directions and Vertical Cutoff Rigidities for a Five Degree by Fifteen Degree World Grid as Calculated Using the

International Geomagnetic Reference Field for Epoch 1975.0, Air Force Geophysics Laboratory Report AFCRL-TR-75-0185, Hanscom AFB, MA, 1975. (NTIS Accession No. AD-A012509)

4.2 Trapped Radiation Belts

4.2.1 Overview

Radiation damage to circuits and materials, background effects in sensors, hazard to personnel, spurious effects in circuits: all are the result of the energetic particle environment. The design of space systems and mission planning and operations require that this energetic-particle environment be considered. The material here is intended to provide an overview in the areas of the dynamics of the particle environment, trapped radiation morphology, current trapped radiation models, and the use of the data supplied in the USAF Space Environment Standard. The references accompanying this discussion can serve as a convenient source for more detailed information in this field.

The Earth's magnetic field contains large fluxes of energetic electrons, protons, and higher-Z (nuclear charge) ions, with energies up to more than 10 MeV for electrons and to over 400 MeV for protons. The source of the electrons and lower energy protons is largely external. Such particles are energized by inward radial diffusion, which is driven by dynamical processes associated with magnetic storms. The high energy protons are the decay product of energetic neutrons produced in the upper atmosphere by collisions of cosmic rays with nuclei of atmospheric atoms and molecules. The magnetospheric energetic-particle population is normally categorized by region and species. Large magnetic storms, with a D_{st} (an index, typically < 0, which is a world-wide average of the change in the low latitude horizontal component of the Earth's magnetic field) > 200 nT in absolute value, produce major perturbations in the magnetospherically-trapped fluxes. Smaller storms, $D_{st} \sim -50$ nT, produce substantially smaller, though still significant, perturbations in the particle fluxes.

For the purpose of discussing the various types of particles and their dynamical behavior, it is convenient to separate the magnetosphere into several regions: the inner zone, $L < 2$ (see *McIlwain's L Parameter* in this section); the outer zone, the region beyond $L > 2.8$; and (for electrons) a slot region. Particle populations in the inner zone are relatively stable. Electron and ring-current ion populations in the outer zone show orders-of-magnitude variations from day to day and week to week in association with magnetic storms. Figure 4.2.1 is a cartoon showing the gross features of the electron regions. Actually, the size of each region varies with particle species and energy. Indeed, the slot region "moves" inward and outward as a result of geomagnetic activity and at times may be totally absent for some electron energies. The data on which Figure 4.2.1 were based included large fluxes of fission electrons in the inner zone. Presently, the inner zone is comprised of electrons with much lower average energy than the outer zone. Figure 4.2.2 is a cartoon depicting the >50 MeV proton fluxes given in AP8. The protons form a single belt in which the typical energy varies inversely with L.

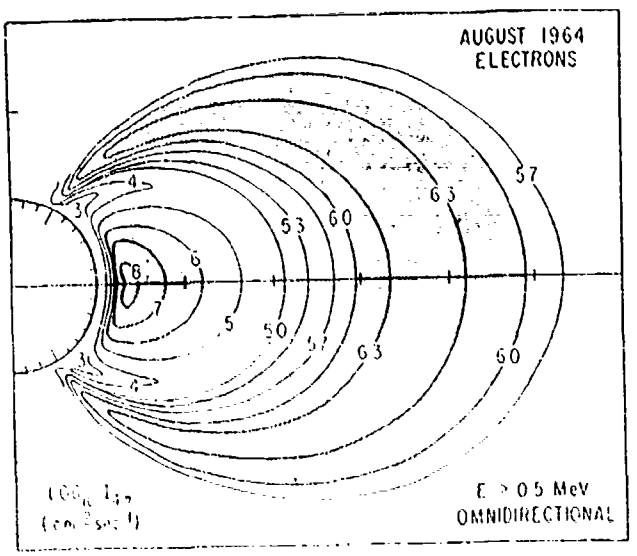

Figure 4.2.1 Cartoon depicting general features of energetic electron belts in the magnetosphere. There are significant fluxes of electrons up to 1.5 MeV in the inner zone and up to 5 MeV in the outer zone. Electrons with energies above 2 MeV in the inner zone and above 10 MeV in the outer zone are present, but do not constitute a significant portion of the total flux.

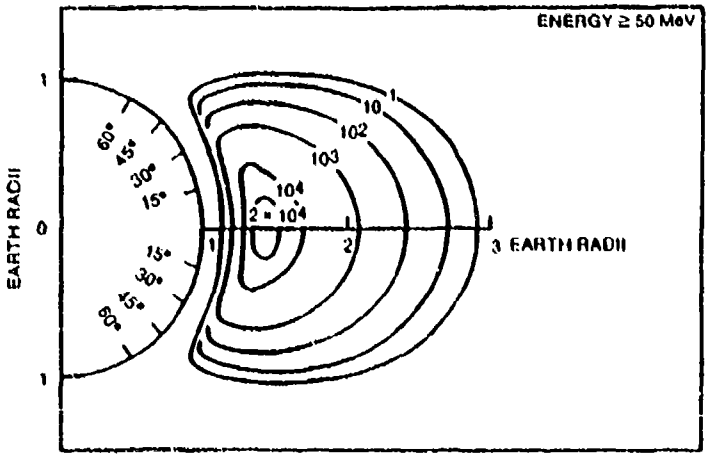

Figure 4.2.2 Cartoon similar to Figure 4.2.1, but depicting general location of the proton belt. Protons with energies >100 MeV peak in intensity near L=1.45. Lower-energy protons peak in intensity at higher L values. However, from a dynamical perspective, it is better to say that the mean energy of a trapped proton varies inversely with L, from a few 10s of keV at L = 8 to 10s of MeV in the inner zone.

McIlwain's L Parameter

A charged particle trapped in the Earth's magnetic field executes three separable motions simultaneously: gyration around the field line, bounce between mirror points in the two hemispheres, and drift in longitude around the world. Figure 4.2.3 depicts these motions. The particle approximately retraces its path as it drifts. The magnetic field intensity B (known as its mirror field, or B_m) is the same at the two ends of its bounce motion . The loci of these mirror points as the particle drifts around the Earth are two rings of constant B_m (one in each hemisphere). As the particle drifts around the Earth, the particle's guiding center traces out a magnetic shell which connects the two rings of mirror points. This shell can be labeled with a constant, L, known as McIlwain's Parameter (Ref. 4.2.1). In a dipole field, the value of L corresponds to the radius of the drift shell, measured in units of Earth radii. In a more realistic field, however, the L value defined by McIlwain (Ref. 4.2.1) has the conceptual disadvantage of not being constant along a field line.

Adiabatic invariants are associated with each of the three particle motions: the first invariant, also known as the magnetic moment of the particle, relates to conservation of Hamiltonian "action" (and thus of the magnetic flux) associated with the orbit of gyration. The second invariant is equal to the action integral associated with the bounce motion between mirror points. The third invariant is proportional to the canonical action associated with the drift motion and thus to the magnetic flux enclosed by the drift shell. This is inversely proportional to L in a dipolar **B** field. A detailed discussion of these invariants is available in Ref. 4.2.3.

Mapping of the particle population in the magnetosphere requires multidimensional labeling: particle species; energy; pitch-angle; altitude, latitude, longitude. The task of mapping the radiation environment is greatly simplified by invoking the adiabatic theory of charged particle motion so as to reduce the spatial variables to two magnetic

coordinates, B and L, which are essentially the drift shells (L) and mirror point trajectories (B_m) described above. All of the particle models discussed below are organized in terms of B, L, and energy.

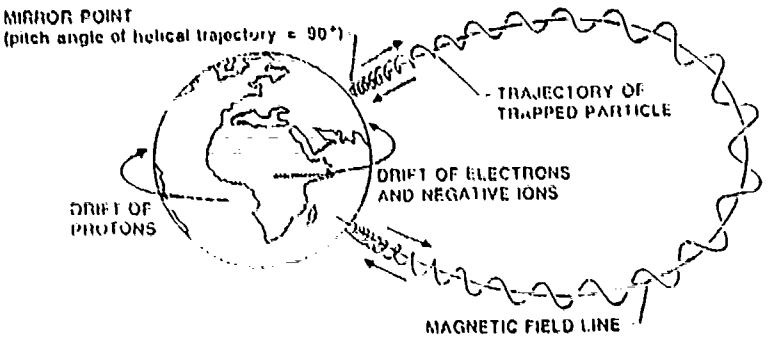

Figure 4.2.3. Charged Particle Motions in the Magnetosphere. Charged particles gyrate around the field line, bounce from one hemisphere to the other, and drift around the world protons westward, electrons eastward).

Inner Zone Electrons

Since the particle models are organized with respect to B and L, and earlier models were specified as to inner or outer zone models, this discussion is organized by zone. The intensity peak for 1 MeV electrons in the inner zone occurs at about L=1.5. In the region $2.0 < L < 2.8$, magnetospheric processes result in a low intensity of energetic electrons during magnetically-quiet periods. At times of large magnetic storms, however, the slot can be "refilled" to rather high flux levels for a few days. The location of the slot is quite variable with time as well as with energy: during large geomagnetic storms, the minimum between the inner and outer radiation belts can be very narrow and may be displaced to a low L value, even centered as low as L=2.0. Immediately after a storm, the slot may be completely filled with electrons. An extensive discussion of these dynamics is available elsewhere (Ref. 4.2.2).

There are few electrons with energies in excess of 1 MeV in the inner zone. Electrons with higher energies are present in small numbers, especially above about L=1.65 after large magnetic storms, but can be ignored as a hazard to space systems except for their background effects in sensors. Inner zone electrons at $L < 1.16$ have lifetimes that are primarily determined by the density of the atmosphere at the mirror points. During solar-active periods, the increased scale height increases the density at a given altitude and thus reduces the lifetimes and lowers the average fluxes. This is reflected in the models by having a solar maximum version and a solar minimum version. Farther out in the inner zone, electrons are quite stable, with typical lifetimes of 400 days per MeV of energy (Ref. 4.2.5) at L=1.5. Principal loss mechanisms at L>1,2 typically involve the pitch-angle scattering of geomagnetically trapped electrons by electromagnetic or electrostatic waves. Pitch-angle scattering alters the local angle between the particle velocity and the field line, thereby changing the mirror altitude. If the mirror altitude of a particle is lowered to below 100 km, then the particle is typically absorbed by the atmosphere

before reaching the next mirror point. Waves responsible for pitch-angle of trapped electrons can be generated by lightning, by ground-based VLF transmitters, and/or by magnetospheric instabilities.

Orders-of-magnitude of the electron fluxes at L=1.45 in the inner zone are as follows: 10^8 for E > 0.1 MeV; 10^6 for E > 1 MeV; 10^5 for E > 2 MeV. These numbers represent integral omnidirectional fluxes, cm^{-2}-sec^{-1}. At L < 1.55 the fluxes are quite stable and show little variation being the solar cycle (Ref. 4.2.7) except for altitudes below 1000 km, at which atmospheric effects are observed. At L > 1.6 major magnetic storms can inject electrons with energies up to at least 1.2 MeV (Ref. 4.2.4).

Outer Zone Electrons

Outer zone electrons have typically entered the magnetosphere from outside (e.g., from the Sun or from Jupiter). Electric field fluctuations (either induced or electrostatic) cause them to diffuse radially inward and energize them in the process. Such energization can be viewed as a consequence of the conservation of the first two adiabatiic invariants during violation of the third (i.e., of the adiabatic invariant associated with azimuthal drift motion). As the particles are transported to field lines deeper in the magnetosphere, the increase in mirror field intensity must be accompanied by an equivalent increase in the square of the particle's momentum, and thus of its energy. When plotted at fixed energy, the various fluxes peak at energy dependent L values, such that the L value of the flux peak varies inversely with electron energy.

The outer electron belt typically peaks around 3.5 < L < 4.0. Significant fluxes of electrons with energies in excess of 5 MeV are observed in the outer zone after major magnetic storms. During extended quiet periods, the outer belt may almost disappear at such high energies. The difference in flux intensity from minimum to maximum can be as high as 5 orders of magnitude (Refs. 4.2.3, 4.2.4) on a given day. Such large

variations are associated with major magnetic storms, for which $D_{st} > 150$ nT. The index D_{st} is an azimuthal average of the horizontal magnetic-field component measured (relative to a baseline)) at several low-latitude observatories. Its variations are attributed mainly to variations in the magnetospheric ring current. This ring current is composed of medium energy ions and electrons (E ~ 10-200 keV) that have been energized by the magnetic storm. Typical decay constants for outer-zone electrons are ~ 10 days per MeV but can be much less during magnetic storms because of storm-associated waves that cause enhanced pitch-angle scattering of the particles into the loss cone. Particles previously trapped on a field line (having mirror points that were above the atmosphere everywhere along their drift paths around the world) can have been perturbed so that they now mirror in the residual atmosphere (below 100 km) at some point along their drift path. A low altitude satellite which normally orbits below the trapped-radiation belts (except when traversing the South Atlantic Anomaly) may suddenly find itself bathed in large fluxes of energetic electrons at mid-latitudes when it encounters these particles which show up (as they are about to precipitate) at low altitudes on outer-zone field lines. The South Atlantic Anomaly is a region of anomalously low magnetic field strength for a given altitude. Since particles mirror at a constant B_m, they attain their minimum mirror-point altitudes here. Representative outer zone fluxes are of the order of: 10^8 for E > 0.1 MeV at L = 6; 10^7 for E > 1 MeV at L = 5; 10^5 for E > 4 MeV at L=4. These numbers represent the integral omnidirectional fluxes, cm^{-2}-sec^{-1}.

Protons

The source of the most energetic protons which are present in the inner zone is ultimately cosmic, in that protons having E > 50 MeV result mainly from the decay of neutrons produced in the upper atmosphere by cosmic rays. The corresponding proton fluxes are quite stable at the equator, but important variations in intensity occur at low altitudes because of variations in atmospheric density with solar activity. Typical intensities are of the order of: 10^4 for E > 100 MeV and 10^3 for E > 300 MeV, both at L = 1.45. Secular variation in the geomagnetic field has led to a significant variation of the energetic proton environment since this was first observed about 30 years ago. This makes it inadvisable to update the (B,L) coordinates of a present-day spacecraft while using an environmental model compiled in terms of yesteryear's (B,L) coordinates. It would almost be better to use the B-field model of 30 years ago to compute the ephemeris of today's spacecraft for this purpose. However, an improved environmental model might alternatively be constructed by following a suggestion of K. A. Pfitzer, viz., that the radiation intensity at a given energy should be modeled as a function of the atmospheric density realized at the minimum mirror-point altitude, regardless of what this implies for variation with respect to B. and L.

Lower-energy protons of most concern are in the 0.5 to 5 MeV range, since there are large fluxes of such particles in both the inner and outer zone. These can have significant effects on surface properties. Particles in this energy range can originate a number of ways: e.g., radial diffusion and consequent energization of solar and other particles which have entered the geomagnetic tail and thence the outer part of the ring current region; auroral acceleration up field lines, with subsequent radial diffusion and concomitant energization; and direct access of solar-flare protons. Typical intensities in the outer zone are: 10^8 for E > 0.1 MeV; 10^7 for E > 1 MeV; > 10^5 for E > 10 MeV; 10^2 for E > 100 MeV. Again, these are omnidirectional integral fluxes in units of cm^{-2}-

sec^{-1}. While the fluxes are subject to variation due to magnetic-storm activity, the variations are much smaller for protons than for electrons. The primary proton loss mechanisms are Coulomb drag (energy degradation through collisions with the residual atmosphere) and (at E < 100 keV) charge-exchange, which results in an energetic neutral particle which is not trapped by the geomagnetic field.

4.2.2 Use of the Standard and Limits of Validity

The flux numbers given in Section 4.1.2 of the Standard refer to the highest flux that will be encountered in the region defined in a given paragraph. If the listed values exceed the survival capability of a system in that particular orbit, more precise calculations should be made by using the referenced NASA particle models. Where two models are listed, MAX and MIN, the MAX and MIN refer to solar-maximum and solar-minimum periods, respectively. Thus, for energetic protons, the MIN model is more severe than the MAX: During solar minimum the atmospheric scale height is smaller, and so energetic protons are removed less effectively by the residual atmosphere. For many orbits, however, there is no difference. All of the models were generated by using DGRF-1964 Epoch 1970 for the magnetic-field calculations. Any use of the models which requires orbital calculations must use the same field model as was used for generating the model flux tables. ONE MUST NOT USE CURRENT FIELD MODELS.

In general, the models are useful over the entire (B,L) range which they encompass. The outer-zone electron models consist of data from low-inclination geosynchronous satellites and high-inclination low-altitude satellites. The models are intended to represent long-term averages, from one-half to a full solar cycle. Data have been extrapolated from low altitude to the equator by using scaling approximations which have not been validated with in-situ data. The result is a significant uncertainty in their ability to correctly predict integrated fluences and doses for long term missions. For short-term missions that are

going to encounter outer zone fluxes, it is not appropriate to rely on models that purport to be solar-cycle averaged. Instantaneous values can be up to two orders of magnitude greater or less than the model flux averages. Short-term averages (up to several weeks) can be greater or smaller than the model fluxes by one order of magnitude.

For very low-altitude satellites, those with orbital altitudes below 500 km, the energetic proton flux encountered can have a strong east-west asymmetry (analogous to the east-west asymmetry of cosmic rays, but contingent on a radial gradient steepened by the atmosphere; see Section 4.2.3 under Proton Models). The proton models do not explicitly include a provision for this effect, but the flux asymmetry is easy to estimate from the gyroradius of the representative particle and the radial gradient of the guiding-center intensity profile.

4.2.3 Models: Utility and Use

Inner Zone Electron Models

The current National Space Science Data Center (NSSDC) models which provide useful inner zone ($1.2 < L < 2.4$) electron data are AE5 (Ref. 4.2.6) for solar minimum, AE6 (Ref. 4.2.7) for solar maximum, and AE8 (Ref. 4.2.8) for either solar minimum or solar maximum. The energy range of these models is from 0.04 MeV to 5 MeV for AE5 and AE6, and 0.04 MeV to 7.5 MeV for AE8. These are empirical models, being based on in-situ measurements of the fluxes. The accuracy of the models is very good, being better than a factor of two for energies below 1 MeV and $L < 1.65$. Present techniques can not make reliable measurements of electrons with energies above 2 MeV at $L < 1.55$ in the inner zone. Above 2 MeV, the fluxes are extrapolations of unknown accuracy. At $L > 1.65$ the variability of the flux levels themselves produces uncertainty. AE8MIN and AE8MAX are the latest models and should be used unless the user is otherwise directed

or unless AE8 is superseded by new models based on new in-situ data.

Outer Zone Electron Models

The current NSSDC outer-zone ($L > 2.4$) model is AE8. The outer zone portion of AE8 is effectively the AE4 model extended from 5 MeV to 7.5 MeV, with some revalidation based on data sets which were not available when AE4 was generated. This model covers the range 0.04 MeV to 7.5 MeV although above 4 MeV it is an extrapolation from lower energy data. For geosynchronous satellites, another model is still relatively valid--AE3 (Ref. 4.2.10), although this model goes up to only 5 MeV and fluxes above 1.5 MeV are all extrapolations. The two versions of AE8, AE8MIN and AE8MAX, differ only in their treatment of the inner zone. The models are probably accurate to a factor of three for dose calculations. Unless the user is otherwise directed, AE8 should be used until it is superseded.

Proton Models

The current proton models are AP8MIN and AP8MAX. These represent the solar minimum and solar maximum periods, respectively. The difference between them reflects the variation with solar activity of the atmospheric density at lower altitudes: At solar maximum the greater scale height of the atmosphere decreases the energetic-proton fluxes. At $L < 2$ the models are probably accurate to 50% or better. They cover the energy range from 0.10 MeV to 400 MeV and the L range from 1.17 to 7. The data were obtained during the same time interval over which the inner zone electron data were obtained. Since the MIN model predicts slightly more flux than the MAX model, it can be used during solar maximum or for long term missions as a conservative model.

A problem occurs because the energetic-proton models are organized in terms of the (B,L) coordinates. The geomagnetic secular variation causes the energetic-proton ensemble, which is nominally very stable, to be carried to lower minimum mirror-point altitudes. The model does not take into account the increased atmospheric density the protons will thus encounter. Consequently, if calculations were made with the magnetic field extrapolated well into the future (more than 10-15 years), then the results obtained for low altitudes such as the Space Station orbit (Ref. 4.2.11) would be totally invalid. Since the source of the energetic protons of interest in this context is the decay of energetic neutrons produced in the upper atmosphere by cosmic rays, the geometry of the production process relative to the atmosphere will not change. The future configuration of the inner-zone proton belt probably will not change relative to the present configuration, provided that both are described in terms of h_{MIN} (= minimum mirror-point altitude of the particle and epoch of interest). One would almost certainly get a more accurate prediction for the proton environment of the Space Station in the year 2025 by making the calculation with the field model and epoch used to generate the particle models (DGRF 1964, Epoch 1970) than by extrapolating the field 35 years into

the future. One could probably get an even better prediction by formulating the environment in terms of the atmospheric density at h_{min}.

For low-inclination, low-altitude orbits (such as used by Shuttle or Space Station so as to minimize exposure to ionizing radiation by staying below the stable trapping region), an additional factor must be considered. For such low orbits the main sources of radiation are the energetic protons in the inner zone, outer-zone electrons after major magnetic storms (if the orbital inclination exceeds 40°), and in polar orbits, solar flare-protons. For almost all such missions the inner-zone protons can be expected to be the primary source of ionizing radiation. At low altitudes the radial gradient in the high-energy proton flux intensity is steep (on account of the exponential variation of atmospheric density with altitude). Protons gyrate about the magnetic field in a left-handed sense. Thus, particles impinging on the west side of a satellite have a guiding-center location above the altitude of the satellite, while those impinging on the east side have a guiding-center location below the satellite. For very energetic protons the radius of gyration can be large compared to the reciprocal of the intensity gradient. Thus, there can be a significantly larger flux incident upon the west side of a low-altitude space vehicle than on the east side. The models do not take this east-west effect into account except to the extent that the flux tables imply a radial gradient. The model fluxes themselves are given in omnidirectional form. Thus, to get a proper estimate of the east-west asymmetry of energetic protons for a low-altitude orbit, one must transform the omnidirectional fluxes to unidirectional fluxes (e.g., as in Ref. 4.2 26 in order to obtain the appropriate radial gradient. Further information on this topic is available in Ref. 4.2.11.

Model Usage

The basic codes include ORB, which is an orbit propagator that provides a listing of longitude, latitude, altitude, B, and L as a function of orbit time; and ORP which uses the

ORB listing as input and does a table look-up for flux as a function of energy, B, and L. Various versions of ORB and ORP have been made available through the years. The current versions are ORB4 and ORP2. Orbit generators other than ORB can be used, provided that they produce an output file of the appropriate format for use by ORP. The orbit generator must be coupled with a magnetic-field model capable of tracing the field line (required for calculation of L, although ORB uses a table look-up for L). ORP then reads the file produced by ORB, does a table look-up for flux, and integrates the flux over the time period produced by the orbit generator. Various outputs (orbital integral, peak flux per orbit, etc.) are available. [An integrated set of codes which does all of the above, SOFIP (Ref. 4.2.13), is also available from NSSCD.] The documentation that comes with the software explains the details. To use the entire package of codes, one selects an orbit and inputs it to ORB, which translates it into residence times in B and L. One then uses the output of ORB as the input to ORP which translates these residence times into total fluence as a function of energy. The output of ORP is then used with SHIELDOSE (Ref. 4.2.12, or a similar energy transport code) to calculate the resulting dose to components as a function of shielding depth on the spacecraft. Any of the models listed above (e.g., AE8MIN) can furnish the flux lookup tables. SHIELDOSE evaluates the energy deposited in Al, H_2O, Si, and SiO_2 as a function of aluminum shielding thickness for three different geometries: semi-infinite plane, center of a solid sphere, and transmission through a finite slab.

4.2.4 Standard Particle Models--Availability

The electron and proton models, and some computer codes for running them, plus SHIELDOSE, are available from the National Space Science Data Center , Code 633, NASA/Goddard Space Flight Center, Greenbelt, MD 20771 (Telephone: 301-286-0536).

Other codes, such as SHIELDOSE, also can be obtained as files on a tape from the National Bureau of Standards, Programming Science and Technology Center, Washington, D. C. 20234. Other sources of the codes are COSMIC and commercial firms (which usually package the codes with a user-friendly interface). All of the codes can be run on VAX computers and on many personal computers. Irrespective of the origin of the software that uses the models, the model flux tables are all obtained from NSSDC. The various models and some of the codes are also available as files on the N3SDCA VAX which is a node on the NASA Science Internet (NSI-DECNet). Thus, anyone with access to DECNet or other networks which can connect to it (such as ARPANET, BITNET, SPRINTnet, etc.) can access these files to download them to a home computer via the network. Alternatively, minor calculations for short checks using these codes can be run interactively on the NSSDCA VAX. An alternate interactive resource is EnviroNET (Ref. 4.2.13), which is resident on a MicroVAX at GSFC and is accessible as the node ENVNET. To access EnviroNET, the user name ENVIRONET and password HENNIKER are used.

4.2.5 References

4.2.1 McIlwain, C. E., Coordinates for Mapping the Distribution of Magnetically Trapped Particles, J. Geophys. Res., 66, 3681-3691, 1961.

4.2.2 Vampola, A. L., Natural Variations in the Geomagnetically Trapped Electron Population, in Proceedings of the National Symposium on Natural and Manmade Radiation in Space, NASA TM X-2440, E. A. Warman, Ed., 1972.

4.2.3 Schulz, M. and L. J. Lanzerotti, Particle Diffusion in the Radiation Belts, Springer, New York, 1974.

4.2.4 Vampola, A. L., J. B. Blake and G. A. Paulikas, A New Study of the Magnetospheric Electron Environment, J. Spacecraft and Rockets, 14, 690, 1977.

4.2.5 Stassinopoulos, E. G. and P. Verzariu, General formula for decay lifetimes of Starfish electrons, J. Geophys. Res., 76, 1841, 1971.

4.2.6 Teague, M. J., and J. I. Vette, The Inner Zone Electron Model AE-5, NSSDC WDC-A-R&S 72-10, 1972

4.2.7 Teague, M. J., K. W. Chan and J. I. Vette, AE-6: A Model Environment of Trapped Electrons for Solar Maximum, NSSDC WDC-A-R&S 76-04, 1976 R&S 72-13, 1972.

4.2.8 Bilitza, D., D. M. Sawyer, and J. H. King, Trapped Particle Models at NSSDC/WDC-A-R&S, this proceedings.

4.2.9 Vette, J. I. and A. B. Lucero, Models of the Trapped Radiation Environment, Vol. III: Electrons at Synchronous Altitudes, NASA SP-3024, 1967.

4.2.10 Baker, D. N., R. D. Belian, P. R. Higbie, R. W. Klebesadel, and J. B. Blake, Hostile Energetic Particle Radiation Environments in Earth's Outer Magnetosphere, in The Aerospace Environment at High Altitudes and its Implications for Spacecraft Charging and Communications, AGARD CP 406, p. 4-1, 1986.

4.2.11 Konradi, A. and A. C. Hardy, Radiation Environment Models and the Atmospheric Cutoff J. Spacecraft and Rockets, 24, p. 284, 1987.

4.2.11a Lemaire,J. A., Roth, Wisemberg, and J. I. Vette, Development of Improved Models on the Earth's Radiation Environment, Institut d'Aeronomie Spatiale de Belgique, 1989

4.2.12 Seltzer, S., SHIELDOSE: A Computer Code for Space Shielding Radiation Dose Calculations, National Bureau of Standards Technical Note 1116,Washington , D.C., 1980.

4.2.13 Stassinopoulos, E. G., J. J. Herbert, E. L. Butler, and J. L. Barth, SOFIP: A Short Orbital Flux Integration Program, NSSDC 79-01, Greenbelt, MD, 1979.

4.2.14 Lauriente, M., EnviroNET: Space Environments for SDIO Experiments, Proceedings of the NASA/SDIO Space Environmental Effects on Materials Workshop, NASA Conference Publication 3035.

4.2.15 Sawyer, D. M., and J. I. Vette, AP-8 Trapped Proton Environment, NSSDC WDC-A-R&S 76-06, 1976.

4.2.17 Vette, J. I., K. W. Chan and M. J. Teague, Problems in Modelling the Earth's Trapped Radiation Environment, AFGL-TR-78-0130, 1978 (NTIS Accession No. AD-A059273).

4.2.18 Vette, J. I., Models of the Trapped Radiation Environment, Volume I: Inner Zone Protons and Electrons (AE-1, AP-1, AP-2, AP-3, AP-4), NASA SP-3024, Washington, D. C., 1966.

4.2.19 Vette, J. I.,A. B. Lucero, and J. A. Wright, Models of the Trapped Radiation Environment, Volume II: Inner and Outer Zone Electrons (AEP-2), NASA SP-3024, Washington, D. C., 1966.

4.2.21 King, J. H., Models of the Trapped Radiation Environment, Volume IV: Low Energy Protons (AP-5), NASA SP-3024, Washington, D. C., 1967.

4.2.22 Lavine, J. P. and J. I. Vette, Models of the Trapped Radiation Environment, Volume V: Inner Belt Protons (AP-6), NASA SP-3024, Washington, D. C., 1969.

4.2.23 Lavine, J. P. and J. I. Vette, Models of the Trapped Radiation Environment, Volume VI: High Energy Protons (AP-7), NASA SP-3024, Washington, D. C., 1970.

4.2.24 Imhof, W. L., C. O. Bostrom, D. S. Beall, C. J. Armstrong, H. H. Heckman, P. J. Lindstrom, G. H. Nakano, G. A. Paulikas and J. B. Blake, Models of the Trapped Radiation Environment, Volume VII: Long Term Time Variations, NASA SP-3024, Washington, D. C., 1971.

4.2.25 Singley, G. W., and J. I. Vette, The AE-4 Model of the Outer Radiation Zone Electron Environment, NSSDC 72-06, Greenbelt, MD 20771, 1972.

4.2.26 Roberts, C. S., On the Relationship Between the Unidirectional and Omnidirectional Flux of Trapped Particles on a Magnetic Field Line of Force, J. Geophys. Res., 70, 2517-2527, 1965.

4.3 Solar Particles

4.3.1 Overview

Major solar flares accelerate solar coronal matter (consisting primarily of protons, helium nuclei, and electrons) and eject it into interplanetary space. The energetic charged particles are constrained by the solar-interplanetary magnetic field, and so their propagation through interplanetary space is anisotropic. They follow interplanetary field lines quite freely but have immediate access only to those that originate on the Sun in the region of the flare. To gain access to other field lines, they must diffuse or drift (Ref. 4.3.5) across the coronal or interplanetary magnetic field.

The solar wind controls the direction of the interplanetary magnetic field Under nominal solar wind conditions typical of flares (Ref. 4.3.6), the Sun will have rotated about 35° between the departure of the solar wind plasma from the Sun and its arrival at the Earth. Thus, the solar magnetic field in the vicinity of the Earth is connected to the Sun near a west solar longitude of 35°. If the flare is situated near this longitude, then the Earth experiences an abrupt arrival of solar-flare protons. For flares at other longitudes, the onset of the solar particle event is more gradual. This is especially so for flares which occur near the eastern limb or on the back side of the Sun. The September 1989 flare location was on the back side of the Sun, but that flare produced the largest energetic-proton fluences seen during the past 35 years.

At geosynchronous orbit solar protons can constitute a major cause of degradation for solar cells and surfaces (thermal coatings). Solar flare protons, even those with relatively low energy (5 - 10 MeV), can gain access to the geosynchronous region via the tail region by gyrating to 6.6 R_e (Ref. 4.3.7). There is evidence that the weakest portion of

the tail field, the neutral sheet, provides preferential access in this way. Once on geomagnetic field lines, solar-flare protons can fill the outer regions of the magnetosphere via diffusion and drift.

Solar-flare protons also have ready access to the polar regions, since most of the geomagnetic tail is formed by field lines from these regions. Thus, satellites in polar or other highly-inclined orbits (such as the Molniya orbit) are also exposed to solar-flare protons. The low-energy portion of the proton spectrum is responsible for surface and solar cell degradation. The high-energy portion of the spectrum contributes to the total dose absorbed by components. It can also cause SEUs and constitute a background in many types of sensors.

4.3.2 Models: Use and Utility

The principal solar proton model in use at this time (Ref. 4.3.1, specified by the Standard) was developed from a statistical study of solar-flare proton events over a solar cycle and from extrapolations of neutron-monitor data on major flare events from the previous solar cycle. A more recent study, utilizing a larger set of events with more detailed data, is also beginning to get some use (Ref. 4.3.2). It was this more recent study which established that the so-called Anomalously Large (AL) events are in fact the high-flux continuation of a log-normal distribution. A recent study (Ref. 4.3.3) of solar protons at geosynchronous altitude for the August 1972 and October 1989 flare events showed that the low-energy end of the flux spectrum is better fitted with a rigidity extrapolation (to the low-rigidity end) than with an energy-spectrum extrapolation.

The data of the Ref. 4.3.1 model are available in a software package (SOLPRO, Ref. 4.3.4) from the National Space Science Data Center, Code 933, Greenbelt, MD 20771.

The model is also available from the same source on the NTS-DECNet node NSSDCA::NODIS. The newer solar proton model, Ref. 4.3.2, is available as a FORTRAN code from the authors.

4.3.3 References

4.3.1 King, J. H., Solar Proton Fluences for 1977-1983 Space Missions, J. Spacecraft and Rockets, 11, 401, 1974.

4.3.2 Feynman, J., and S. B. Gabriel, A New Model for the Calculation and Prediction of Solar Proton Fluences, AIAA Paper 90-0292, 1991.

4.3.3 Lanzerotti, L. J., D. W. Maurer, H. H. Sauer, and R. D. Zwickl, Large Solar Proton Events and Geosynchronous Communication Spacecraft Solar Arrays, to be published in the Journal of Spacecraft and Rockets, 1991.

4.3.4 Stassinopoulos, E. G., SOLPRO: A Computer Code To Calculate Probabilistic Energetic Solar Proton Fluences, NSSDC 75-11, Greenbelt, MD 20771, 1975.

4.2.5 Mullan, D. J., and K. H. Schatten, Motion of Solar Cosmic Rays in the Coronal Magnetic Field, *Solar Phys.*, *62*, 153-177, 1979.

4.3.6 Parker, E. N., Dynamics of the Interplanetary Gas and Magnetic Fields, *Astrophys. J.*, *128*, 664-675, 1958.

4.3.7 Paulikas, G. A., and J. B. Blake, Penetration of Solar Protons to Synchronous Altitude, *J. Geophys. Res.*, *74*, 2161-2168, 1969.

5. Gravitational Field

5.1 Overview

The Earth's gravitational potential is described adequately by WGS 84. The coefficients for WGS84 are presented at the end of this section. For planning purposes and other non-critical uses, the model can be truncated (even to as low as order-4 coefficients for some purposes) and still maintain satisfactory accuracy. Useful equations are presented below.

Earth's Gravitational Potential

The Earth's gravitational potential can be expressed in the form:

$$V = Gm_e/r\left[1+\sum_{n=2}^{nmax} S_{m=0}^{n} (a/r)^n P_{n,m}(\sin f')(C_{n,m}\cos ml + S_{n,m}\sin ml)\right]$$

where symbols are as above and

r = radius vector from the Earth's center of mass

m, n = degree and order, respectively

f' = geocentric latitude

$C_{n,m}$ and $S_{n,m}$ = normalized gravitational coefficients

$= [(n+m)!/(n-m)!(2n+1)k]^{1/2} \times C_{n,m}$ and $S_{n,m}$

where $C_{n,m}$ and $S_{n,m}$ are the conventional gravitational coefficients.

(see Table 8.1 for $C_{n,m}$ and $S_{n,m}$)

$k = 1$ for $m=0$

$k = 2$ for $k>0$

$P_{n,m}$ = normalized associated Legendre polynomial

$$= [(n-m)!(2n+1)k/(n+m)!]^{1/2} \times P_{n,m}$$

$P_{n,m}(\sin f')$ = associated Legendre polynomial

$$= (\cos f')^m \frac{d^m (\sin^2 f' - 1)^n [P_n(\sin f')]}{d(\sin f')^m}$$

and $P_n(\sin f')$ is the regular Legendre polynomial

$$= 1/(2^n n!) \frac{d^m (\sin^2 f' - 1)^n}{d(\sin f')^m}$$

Orbital Period:

$T = 2\pi \sqrt{(a^3/Gm_e)}$ $= 3.1471 \times 10^{-7}\ a^{3/2}$ seconds

where G = gravitational constant, $6.673 \times 10^{-11}\ m^3\ kg^{-1}\ s^{-2}$

m_e = mass of the Earth, 5.9733328×10^{24} kg

a = semi-major axis (= r_e + altitude in meters for circular orbits)

r_e = Earth semi-major axis (6378137 m)

and nautical mile = 1852 m

statute mile = 1609.344 m

Orbital Elements:

Keplerian.

i	Inclination
a	Semi-major axis
e	Eccentricity
Ω	Right ascension of the ascending node
t_o	Epoch time
$\nu\cdot$	Precession of perigee [$= 5(5\cos^2 i - 1)/a^{7/2}(1-e^2)^2$ deg/day]
$\Omega\cdot$	Precession of the ascending node[$= -10\cos i/a^{7/2}(1-e^2)^2$ deg/day]

5.2 References

5.1 WGS 84: Defense Mapping Agency, Department of Defense World Geodetic System 1984, Its Definition and Relationships with Local Geodetic Systems, (WGS 84) DMA TR-8350.2, 30 Sept. 1987.

5.2 Lerch, F. J., S. M. Klosko, R. E. Laubscher, and C. A. Wagner, Gravity Model Improvement using GEOS-3 (GEM 9 and 10), *J. Geophys. Res.*, *84*, 3897-3916, 1976.

6. Meteoroids

6.1 Overview

The meteoroid environment has always been an important consideration in the design of satellites and spacecraft. At any given time, approximately 200 kg of meteoroid material is traveling through the region of space below 2000 km altitude. Most of the particles of interest are ~ 0.1 mm in diameter and are traveling at an average velocity of 20 km/sec. (Since the distribution of meteoroid diameters is logarithmic, there are far fewer meteoroids of larger size; smaller meteoroids are unlikely to do any significant damage except to optical surfaces.) The meteoroid population down to 1 mm is known from ground-based observations. Below this size, additional information has been obtained from the return of surfaces from various satellites such as Solar Maximum Mission and from in-situ measurements by satellites such as Pegasus. Additional information has recently become available from the retrieval of the Long Duration Exposure Facility (LDEF). The in-situ data are limited to low-altitude orbits (under 500 km).

In Earth low orbit, the primary constituent is not meteoroids, however, but debris, traveling at velocities ~7 km/sec. From an operational point of view, the difference between debris and meteoroids is significant. Although an impact from either will result in a crater with a diameter that is typically 10 times that of the impacting particle, the difference in relative velocity causes a completely different pattern of impacts on the satellite. Meteoroids, with typical velocities of 20 km/sec compared to the 7-10 km/sec velocities of LEO satellites, have only a very small asymmetry in direction of approach. Debris, on the other hand, has a velocity approximately equal to LEO satellites. Actual impact velocity for intersecting orbits are somewhat higher, and most impacts from debris occur on the ram face of a satellite, with a small number of impacts perpendicular to the orbit plane. Very few debris impacts occur on the wake surface of a satellite. In

very low orbit, most impacts are by very small particles (0.1 micron diameter) which are falling very slowly through the upper atmosphere, and thus are run into by the satellite. Most of these debris particles have resulted from fluid dumps during manned space flights or from combustion products emitted by solid rocket motors. A small fraction have resulted from previous impacts on the same satellite (e.g., the majority of impacts on SMM were paint particles, ZOT, from SMM). In general, such debris is concentrated in those few types of orbits that are in most use (e.g., low altitude reconnaissance, low altitude weather observation, geosynchronous communication, etc.)

The concentration of meteoroids is relatively constant (except for minor increases during periods when the Earth passes through known meteoroid concentrations, such as the Perseids). The number of debris particles, on the other hand, is continually increasing. Although Mil Std 1801 addresses only the natural environment, the debris population must also be considered. Ref. 6.5 gives impact probability estimates and shielding requirements for low Earth orbit. Figures 6.1 and 6.2 are from Ref. 6.5.

Figure 6.1. Detectability limitations of the US Space Command sensor system.

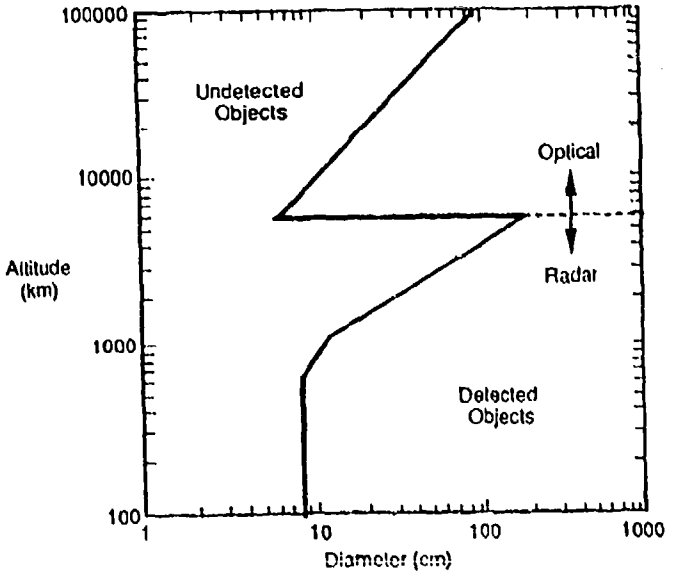

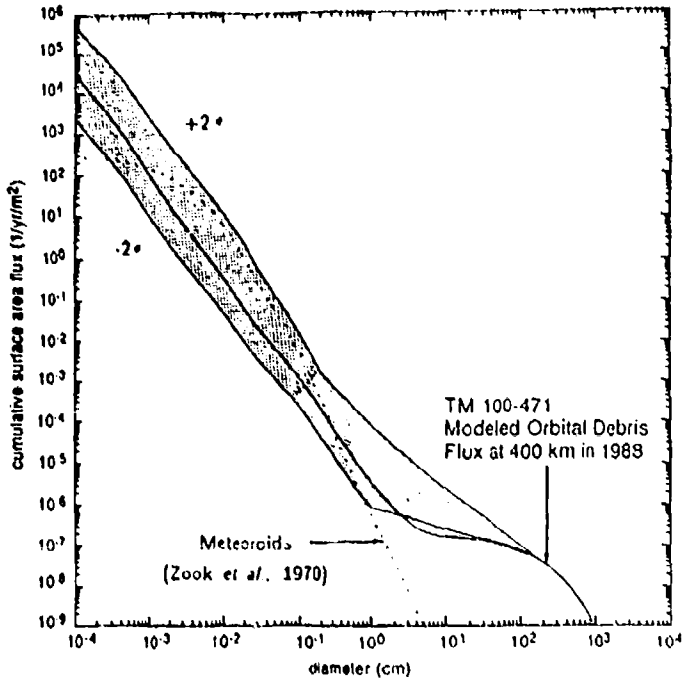
+2σ
-2σ
TM 100-471
Modeled Orbital Debris
Flux at 400 km in 1988
Meteoroids
(Zook et al., 1970)
cumulative surface area flux (1/yr/m²)
diameter (cm)

(a)

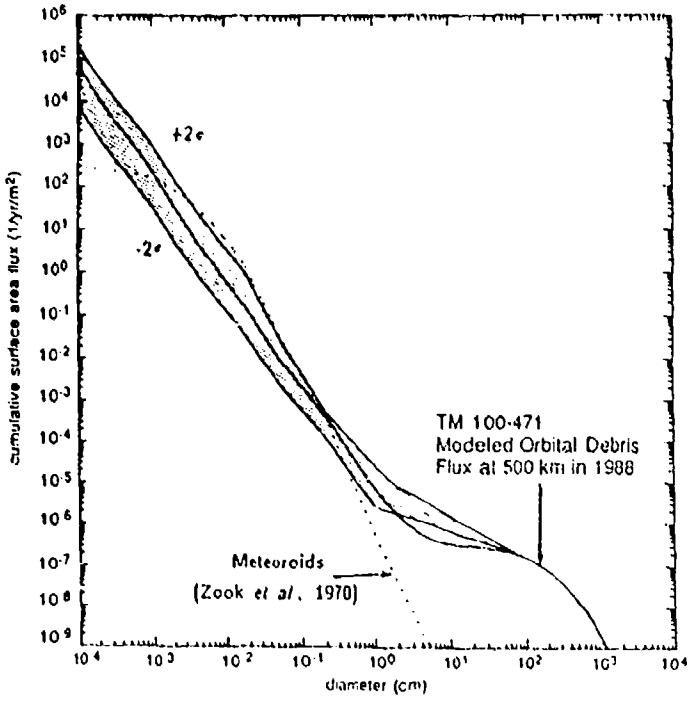
+2σ
-2σ
TM 100-471
Modeled Orbital Debris
Flux at 500 km in 1988
Meteoroids
(Zook et al., 1970)
cumulative surface area flux (1/yr/m²)
diameter (cm)

(b)

Figure 6.2. Uncertainties in the current environment at 400 and 500 km compared to the values presented in NASA TM 100-471 (Ref. 6.4)

6.2 References

6.1. USAF Advisory Board, Current and Potential Technology to Protect Air Force Space Missions from Current and Future Debris, December 1987.

6.2 Howell Jr., L. W., A Stochastic Model for Particle Impingements on Orbiting Spacecraft, J. Astro. Sci., 34, No. 4, Oct-Dec 1986, pp. 375-401.

6.3 Meteoroid Environment Model-1969, NASA SP 8013, 1969.

6.4 Kessler, D. J., R. C. Reynolds, and P. D. Anz-Meador, Orbital Debris Environment for Sp[acecraft Designed to Operrate in Low Orbit, NASA Tech. Memo. 10471, NASA/JSC, Houston, 1989.

6.5 Kessler, D. J., Orbital Debris Environment for Spacecraft in Low Orbit, J. Spacecraft and Rockets, 28, 1991.

7. Solar Radiations

7.1 Overview

The Sun can be characterized as a blackbody radiator with a temperature of 5800° K. The output in the visible and IR range is quite constant (variation of the order of 0.1%) but is quite variable in the EUV and in X-Rays. The variation is due to sunspot coverage, rather than variations in temperature. While the area covered by sunspots can reach a few percent, this does not result in that large a change in the solar output. The sunspots are very hot and radiate quite well. They are dark only in relation to the surrounding area.

At radio frequency (10.7 cm), the variability follows the EUV variability. The 10.7 cm flux ($F_{10.7}$ parameter) is used as a proxy for the EUV radiation because the atmosphere is transparent to 10.7 cm wavelengths and ground based measurements are easily made. The EUV is absorbed in the upper atmosphere, heating it. The result of the heating is an increase in scale height of the atmosphere, and a resulting increase in drag on low altitude (<1000 km) satellite. The increase in drag during a very solar active period can be very significant. During high solar activity, orbital predictions based on average atmospheric scale heights have resulted in temporarily losing track of low altitude satellites. The average albedo of the Earth is 0.3, with the same spectrum as the solar input. For short times (minutes to hours), the albedo can vary from one-half to twice this value. Variations in cloud cover produce the variations in albedo. Note that this albedo is not to be confused with the thermal radiation of the Earth itself, which is characterized as a blackbody radiation at 288° K. The thermal radiation averages about 230 W/m^2, but on a short time scale can vary from 140 to 270 W/m^2. The average solar constant at 1 AU is 1371 W/m^2.

For systems that are light sensitive, in addition to the solar output, Earth albedo, and Earth thermal radiation, two other natural sources of visible light must be considered. In low altitude orbits (up to perhaps 700 km), surfaces exposed to the atmospheric ram produce a glow. This is thought to be due to surface chemistry associated with the high energy nitrogen and atomic oxygen impacts. In the auroral regions, particle precipitation associated with auroral electric fields also produce visible light. In both instances, the emissions have a line or band structure.

7.2 Models

Both infrared and ultraviolet models are available, though not officially sanctioned by any international body. The high resolution catalog of the infrared spectrum (from 650 to 4800 cm^{-1}) of the Sun (Volume 1, Ref. 761 and of the Earth's atmosphere (Volume 2, Ref. 7.2) was prepared using data from the Atmospheric Trace Molecule Spectroscopy (ATMOS) experiment on Spacelab 3. The catalog is available from NASA.

The SERF2 Solar EUV Flux model (Ref. 7.3), which was developed from satellite and rocket data, is in a preliminary stage, though it is being updated as new data become available.

7.3 References

7.1 Farmer, C. B., and R. H. Norton, A High Resolution Atlas of the Infrared Spectrum of the Sun and the Earth Atmosphere from Space, Volume I. The Sun (650 to 4800 cm^{-1}), NASA Reference Publication 1224, Washington, D.C., 1989.

7.2 Farmer, C. B., and R. H. Norton, A High Resolution Atlas of the Infrared Spectrum of the Sun and the Earth Atmosphere from Space, Volume II. Stratosphere and Mesosphere (650 to 3350 cm^{-1}), NASA Reference Publication 1224, Washington, D.C., 1989.

7.3 Tobiska., W. K.., and C. A. Barth, A Solar EUV Flux Model, J. Geophys. Res. 95, 243, 1990.